NANO LETTERS

Letter

pubs.acs.org/NanoLett

Tunable GaTe-MoS_2 van der Waals p−n Junctions with Novel Optoelectronic Performance

Feng Wang,[†,‡] Zhenxing Wang,[†] Kai Xu,[†,‡] Fengmei Wang,[†,‡] Qisheng Wang,[†,‡] Yun Huang,[†,‡] Lei Yin,[†,‡] and Jun He*,[†]

[†]CAS Key Laboratory of Nanosystem and Hierarchical Fabrication, National Center for Nanoscience and Technology, Beijing 100190, China

[‡]University of Chinese Academy of Sciences, No. 19A Yuquan Road, Beijing 100049, China

Supporting Information

ABSTRACT: P-n junctions based on vertically stacked van der Waals (vdW) materials have attracted a great deal of attention and may open up unforeseen opportunities in electronics and optoelectronics. However, due to the lack of intrinsic p-type vdW materials, most previous studies generally adopted electrical gating, special electrode contacts, or chemical doping methods to realize p-n vdW junctions. GaTe is an intrinsic p-type vdW material with a relatively high charge density, and it has a direct band gap that is independent of thickness. Here, we report the construction of ultrathin and tunable p-GaTe/n-MoS_2 vdW heterostructure with high photovoltaic and photodetecting performance. The rectification ratio, external quantum efficiency, and photoresponsivity are as high as 4×10^5, 61.68%, and 21.83 AW^{-1}, respectively. In particular, the detectivity is up to 8.4×10^{13} Jones, which is even higher than commercial Si, InGaAs photodetectors. This study demonstrates the promising potential of p-GaTe/n-MoS_2 heterostructures for next-generation electronic and optoelectronic devices.

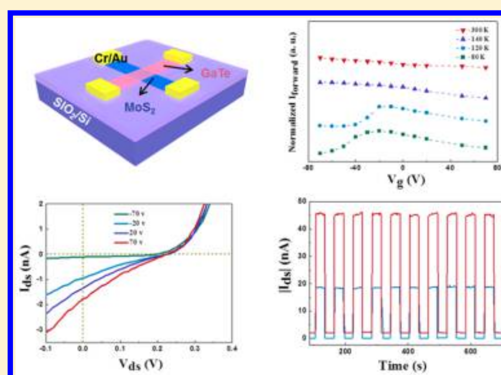

KEYWORDS: *GaTe, MoS_2, van der Waals heterostructure, photovoltaic effect, photodetection*

Recently, new research has focused on two-dimensional van der Waals heterostructures (2D vdWHs), in which individual two-dimensional layered materials (2DLMs) are artificially stacked on the top of each other in a given sequence.[1−5] Because they are ultrathin and unrestricted by lattice matching, 2D vdWHs may have a fundamentally new mechanism and notable performance.[1,2,6−10] For example, unlike in conventional p−n junctions that form built-in potentials, interlayer recombination may determine the rectification characteristics and photovoltaic (PV) effects exhibited in atomically thin MoS_2/WSe_2 heterostructures.[6] Furthermore, 2D vdWHs always show strong light−matter interaction because (a) elementary 2DLMs either have an intrinsic direct band gap or exhibit an indirect−direct band gap transition while scaling down to a monolayer,[11−13] (b) most 2DLMs can form a type II bang gap alignments when brought into contact,[14,15] and (c) their two-dimensional configuration gives them ultrahigh specific surface areas. Considering MoS_2/WS_2 as an example, it takes only 50 fs for photostimulated holes to transfer from the MoS_2 to the WS_2 layer.[16] Because of their extraordinary properties, 2D vdWHs have been studied as PV and photodetectors.[17−20,4] In addition, due to their ultrathin thickness and steep interfacial charge-carrier gradient, 2D vdWHs show strong electrical tunability for electronic and optoelectronic properties.[6,21−23]

Until now, several 2D vdWHs, including p-WSe_2/n-MoS_2, WS_2/MoS_2, p-MoS_2/n-MoS_2, and black phosphorus (BP)/MoS_2, have been investigated for electronic and optoelectronic applications.[6,21−24] Due to the outstanding properties of MoS_2, such as intrinsic n-type characteristics, a direct band gap of 1.9 eV in a monolayer,[11] high electron mobility,[25,26] and photoresponsiveness,[27−30] it is the most commonly used electron provider in 2D vdWHs. However, because of the lack of intrinsic p-type 2DLMs, most previous studies generally adopted additional measures, such as electrical gating, special metal contact, or chemical doping methods to create p−n junctions,[17,18,20,31,32] which are undesirable for practical applications of vdW p−n junctions. For instance, because of their ambipolar characteristics, WSe_2, $MoTe_2$, and black phosphorus need electrical gating or particular electrode contacts (like Pd for WSe_2) to obtain p-type properties.[3,17,24,33] In another study, to obtain p-type MoS_2, a complex chemical doping process must be involved for its strong Fermi level pinning effect,[20] which could degrade the carrier mobility as a result of scattering from the dopant. It is therefore imperative to design new p-type 2DLMs to realize any practical

Received: August 17, 2015
Revised: October 14, 2015

 © XXXX American Chemical Society

DOI: 10.1021/acs.nanolett.5b03291
Nano Lett. XXXX, XXX, XXX−XXX

applications of 2D vdW p−n junctions. Recently, our group has systematically studied and found that GaTe is an intrinsic p-type 2DLM with high hole density of 6×10^{12} cm^{-2}.[34] Furthermore, it has been demonstrated that GaTe exhibits a direct band gap independent of thickness (1.7 eV for multilayer), which gives few-layer GaTe phototransistors a high photoresponsivity of 10^4 A W^{-1} and a fast response time of 6 ms.[35] All of these features make GaTe a promising building block for the construction of 2D vdW p−n junctions as a p-type 2DLM.

Here, we demonstrate a tunable p-GaTe/n-MoS_2 vdW p−n junction. The current rectification, PV and photodetection capabilities are systematically investigated under various temperatures, electrical gate bias conditions, and light intensities. The p−n junctions showed strong gate- and temperature-tunable rectification characteristics. The highest rectification ratio (RF) of 4×10^5 was achieved at 140 K, V_g = −40 V and V_{ds} = ± 1 V. Under illumination, an obvious PV effect with an external quantum efficiency (EQE) as high as 61.68% was observed. We also found that the Shockley Read Hall (SRH) recombination mechanism dominated the interlayer recombination,[6,21,36,37] and a negative temperature gradient of $(dV_{oc}/dT) \approx -0.7$ mV/K was recorded. Futhermore, the GaTe/MoS_2 p−n junction exhibited high photoresponsivity (21.83 A W^{-1}) and photogain (5737%) at room temperature. Remarkably, a specific detectivity of 8.4×10^{13} Jones was achieved, which is even higher than commercial Si/InGaAs photodetectors.[38,39]

The devices were fabricated by mechanical exfoliation and targeted transfer method (see methods for detail).[40] Briefly, few-layer MoS_2 was first exfoliated onto SiO_2/Si wafers and annealed in vacuum to remove any residue tapes. GaTe was then separately exfoliated on the top of poly(vinyl alcohol)/poly(methyl methacrylate) (PVA/PMMA) film. After dissolving PVA, PMMA film carrying exfoliated GaTe was mounted on the arm of micromanipulator and transferred directionally onto the target MoS_2 flake. PMMA was then dissolved with acetone. Finally, the heterostructure was annealed again in vacuum to eliminate the possible contamination from the GaTe/MoS_2 interface. Electron-beam lithography (EBL) was used to define the electrode patterns, and 8/60 nm Cr/Au electrodes were deposited by thermal evaporation. The schematic and optical microscope (OM) images of the device are shown in Figures 1a and S2a (Supporting Information), respectively. From the transfer curves of independent MoS_2 and GaTe (Figure S3a, Supporting Information), we can infer the respective densities of majority charge carriers (electrons for MoS_2 and holes for GaTe) to be 7.5×10^{11} cm^{-2} for both materials, giving differences between the Fermi levels (E_F) and the conduction band edge (for MoS_2)/valence band edge (for GaTe) of approximately 0.41 and 0.37 eV at T = 300 K, respectively (see Supporting Information for calculation details). Hence, as shown in Figure 1b, the E_Fs of GaTe and MoS_2 are estimated to be 4.53 and 4.41 eV below the vacuum level, respectively. As a consequence, a vdW p−n junction with a type II band alignment formed in the overlapping region of the device, which may promote the charge separation and enhance the optoelectronic performance.[6,9,10,41] In addition, to reduce the Schottky barrier at the semiconductor/electrode interfaces, Cr with a matched work function (see Figure 1b) was used as the electrode metal.[42] As a result, the discovered properties arise mainly from the p−n junction region, as recently confirmed in the literature.[6,10] As shown in the atomic force microscope (AFM) image (Figure 1c), the device was combined with few-layer MoS_2 and GaTe with a thickness of 5.5 and 14.1 nm, respectively. Notably, the uniform contrast that can be observed in the overlapping region demonstrates good contact between the two flakes. The Raman spectra (see Supporting Information, Figure S2b,c) further confirm the quality of our device after the fabrication process. The corresponding spatially resolved Raman maps of GaTe (at Raman shift of 145 cm^{-1}) and MoS_2 (at Raman shift of 408 cm^{-1}) are presented in Figure 1d.[28,43] Due to the strength weakening (Figure S2b,c, Supporting Information), Raman quenching in the overlapping region was observed, which can be attributed to the interference between the two flakes due to van der Waals forces. The uniform quenching further demonstrates good contact at the van der Waals junction.

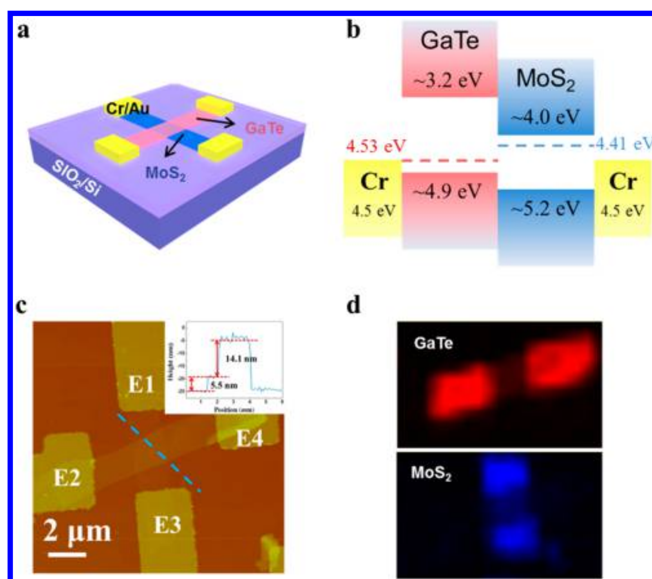

Figure 1. (a) Schematic of our GaTe/MoS_2 van der Waals p−n junction. GaTe was exfoliated on the top of the MoS_2 flake, and 8/60 nm Cr/Au was used as electrodes. (b) Band diagrams for GaTe (left red bands), MoS_2 (right blue bands), and Cr contact (yellow). The estimated positions of conduction and valence band edges for GaTe and MoS_2 as well as the work function of Cr are provided. A type II band gap alignment formed while GaTe and MoS_2 were in contact. (c) AFM image of the device. The four electrodes are marked as E1, E2, E3, and E4. Inset: a line scan along the dashed blue line shown in c. (d) Spatially resolved Raman maps for the GaTe (top panel, Raman shift at 145 cm^{-1}) and the MoS_2 (bottom panel, Raman shift at 408 cm^{-1}).

For further insight into the device's performance, temperature- and gate-variable electrical characterizations were conducted between electrodes E1 and E2, as shown in Figure 1c. Figure 2a−d shows the current−voltage (I_{ds}−V_{ds}) curves as a function of the gate voltage (V_g) measured at 80, 120, 140, and 300 K, respectively. Like a conventional diode, our device showed an obvious current rectification capability under all test conditions. The rectification behavior can be observed more clearly in the log scale I_{ds}−V_{ds} curves shown in Figure S4 (Supporting Information). Furthermore, owing to the ultrathin thickness of the p−n junction and the sharp charge carrier gradient at the interface, the I_{ds}−V_{ds} characteristics can be strongly tuned by V_g. Specifically, at 80 K (Figure 2a), a maximum drain current under a 1 V forward bias ($I_{forward}$) appeared at V_g = −20 V. A similar trend can be observed at 120 K (Figure 2b). However, as T increased to 140 and 300 K,

DOI: 10.1021/acs.nanolett.5b03291
Nano Lett. XXXX, XXX, XXX−XXX

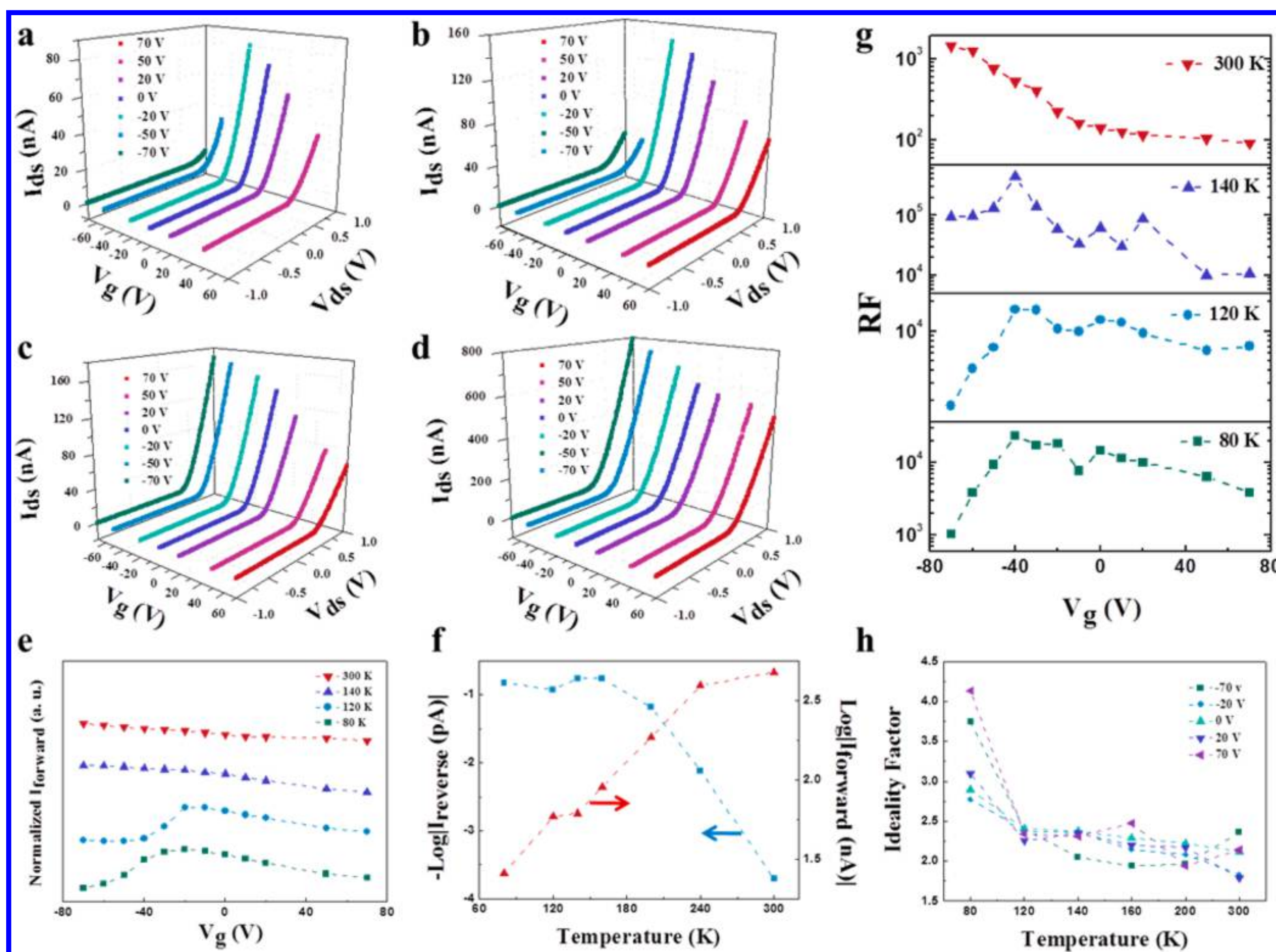

Figure 2. Drain current−voltage characteristics at various gate voltages measured at (a) 80, (b) 120, (c) 140, and (d) 300 K, respectively. Measurements were taken between electrodes 1 and 2 (E1 and E2 shown in Figure 1c). (e) The normalized drain current (V_{ds} = 1 V) at various temperatures as a function of the gate voltage (extracted from a−d). (f) Relationships between the forward current (red symbols, V_{ds} = 1 V)/reverse current (blue symbols, V_{ds} = −1 V) and temperature at V_g = 70 V. (g) Relationships between the rectification ratio (defined as RF = $I_{forwad}/I_{reverse}$) and the gate voltage at different temperatures. (h) Ideality factors (IF) as a function of temperature measured at various gate voltages.

$I_{forward}$ decreased linearly with V_g, reaching a maximum value at V_g = −70 V. To show the effect more clearly, Figure 2e (extracted from Figure 2a−d) summarizes the relationships between the normalized $I_{forward}$ and V_g at various temperatures. A similar temperature-induced change in the relationship between I_{ds} and V_g can also be observed in the transfer curves measured at 80 and 300 K (see Supporting Information, Figure S3b,c). This change in the relationship between $I_{forward}$ and V_g is probably due to the effect of temperature on the gate-tunability of carriers in GaTe (see below). Figure 2f depicts the reverse ($I_{reverse}$, V_{ds} = −1 V) and forward ($I_{forward}$, V_{ds} = 1 V) drain currents at V_g = 70 V as a function of temperature (T) on a logarithmic scale. Both of the drain currents increase monotonically with T, which is probably because (a) the carrier conduction in 2D materials is typically governed by the variable range hopping (VRH) mechanism, which is thermally activated, so the carriers experience an increasing mobility with increasing T;[44] (b) the thermally activated carrier densities increase; and (c) the built-in potentials of the van der Waals p−n junction decrease (Figure 3, see below). A similar trend was also found for other gate voltages (see Supporting Information, Figure S4e). Combining $I_{forward}$ and $I_{reverse}$ by defining rectification ratio, RF = $I_{forward}/I_{reverse}$, the relationship with V_g showed a similar trend with T: the RF reaches a maximum at V_g = −40 V for 80, 120, and 140 K, while the curve for 300 K is monotonic (Figure 2g). A highest RF of 4 × 10^5 was obtained at 140 K, V_g = −40 V, and V_{ds} from −1 to 1 V. Interestingly, a valley point is observed at about V_g = −10 V in Figure 2g for 80, 120, and 140 K, which is probably owing to the inconsistency of relationships between the $I_{forward}-V_g$ and $I_{reverse}-V_g$ (see Supporting Information for details).

From a structural point of view, the device can be seen as a series connection of isolated GaTe and MoS_2 parts and the overlapped junction region. Considering the observations above, which indicate that the charge transport can be modulated by the gate voltage and temperature, it is the junction region that dominates the transport properties[6,21,22] that can be understood using the band diagrams of the van der Waals p−n junction under various conditions. Based on the estimated band positions of GaTe and MoS_2 shown in Figure 1b, the band diagrams under forward bias are presented in Figure 3a (T > 140 K) and b (T < 140 K). Due to the built-in potential, arising from the difference in the carrier densities between two semiconductors, rectification behavior was induced at both temperatures. Before applying the gate voltage (middle column), the built-in potential was determined solely

DOI: 10.1021/acs.nanolett.5b03291
Nano Lett. XXXX, XXX, XXX−XXX

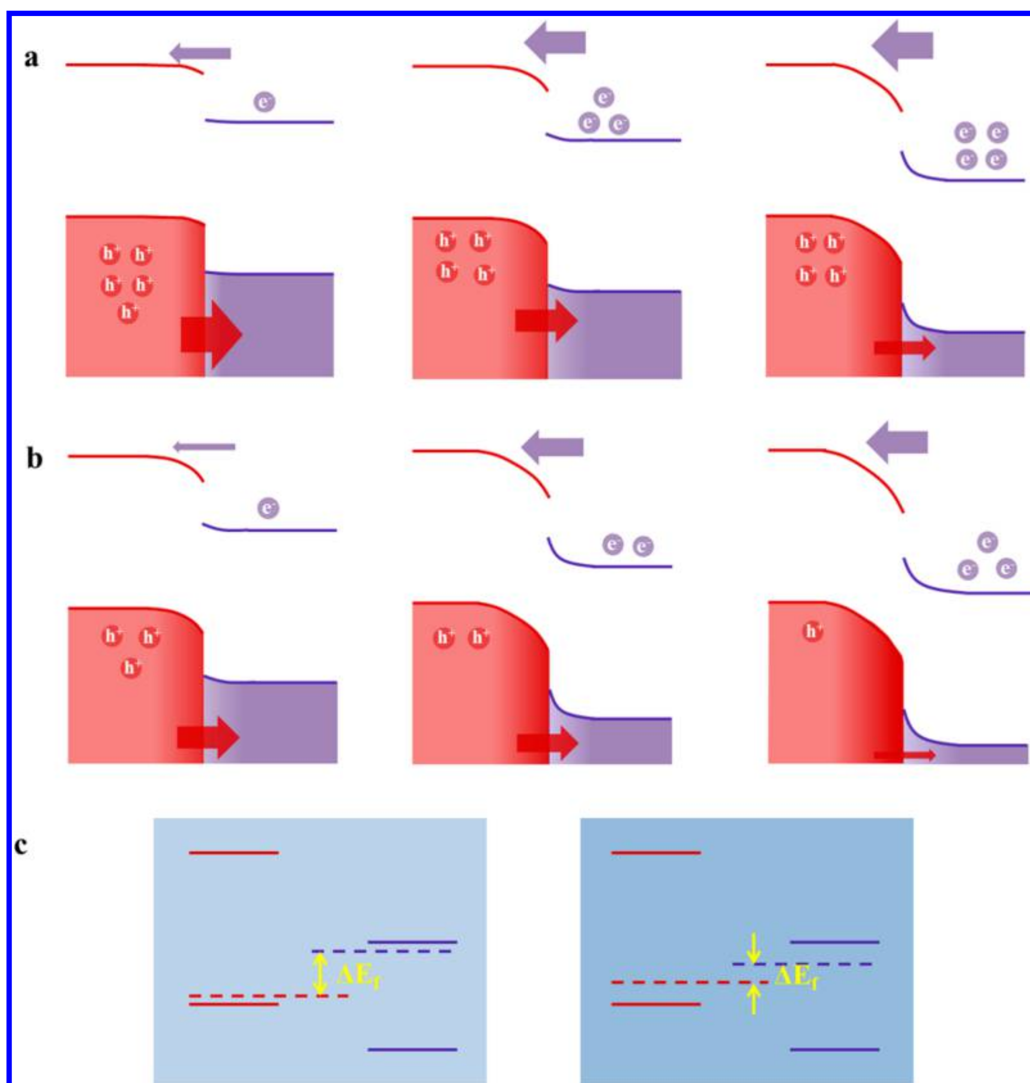

Figure 3. Schematic band diagrams of the heterostructure with negative (left), zero (middle), and positive (right) back gating under forward bias at the temperature of (a) >140 K and (b) <140 K. Red and purple lines represent the band diagrams of p-GaTe and n-MoS_2. Red and purple circles indicate holes and electrons in GaTe and MoS_2 respectively. The diffusion current of the majorities under forward bias are marked as arrows. (c) Band gap alignments of GaTe (red) and MoS_2 (purple) at 80 K (left) and 300 K (right) before contact. Dotted lines represent the respective Fermi levels (E_F), with the differences marked as ΔE_F.

by the intrinsic Fermi levels (E_F). While at negative (left column) or positive (right column) V_g, the built-in potential will be modulated to smaller or larger values because of the stronger gate-tunability of the underneath MoS_2 than the upper GaTe.[18] Along with the weak carrier density-gate dependence of GaTe at high temperatures (and the smaller built-in potential under a negative V_g),[27] the $I_{forward}$ increased linearly with decreasing V_g at T > 140 K (Figure 3a). However, due to the inhibition of thermal activation at low temperatures (Figure 3b), the charge densities were reduced and became the limiting factor to determine the current values. In that case, the applied V_g reduces the densities of either the holes in GaTe (at positive V_g) or the electrons in MoS_2 (at negative V_g). As a result, a maximum $I_{forward}$ was observed at V_g = −20 V, where both diffusion currents of electrons and holes had a moderate nonzero value. In addition, taking the nonoverlapping GaTe and MoS_2 parts into account, the V_g-tunable rectification behavior is strengthened or weakened at low or high temperature, respectively. Specifically, for T < 140 K condition, GaTe or MoS_2 can be turned off under positive or negative gate voltage, which strengthens the peak in the trend of $I_{forward}-V_g$ curve. However, at T > 140 K, the monotonic trend of $I_{forward}$ is weakened, indicating the predominant role of the junction region in the transport behavior. It is noteworthy that the temperature at which the trend changes agrees highly with the temperature at which Ga vacancies are activated in GaTe,[27] indicating that the temperature-dependent properties of GaTe played a decisive role in the V_g- and T-tunable rectification behavior of the p−n junction. From the ideality factors (IF)-T characteristics at various gate voltages shown in Figure 2h and Figure S3d (Supporting Information),[45] it is evident that the van der Waals junction exhibited a larger deviation from an ideal diode at low temperature for each V_g. This trend indicates that the recombination between holes on the valence band maximum (VBM) of GaTe and electrons on conduction band minimum (CBM) of MoS_2 that occurred at the heterointerface probably played a crucial role on the charge transport behavior at low T, similar to what has been observed in MoS_2/WSe_2 van der Waals heterostructure.[3] However, unlike the monolayer thickness used in ref 3, our van der Waals p−n junction was

DOI: 10.1021/acs.nanolett.5b03291
Nano Lett. XXXX, XXX, XXX−XXX

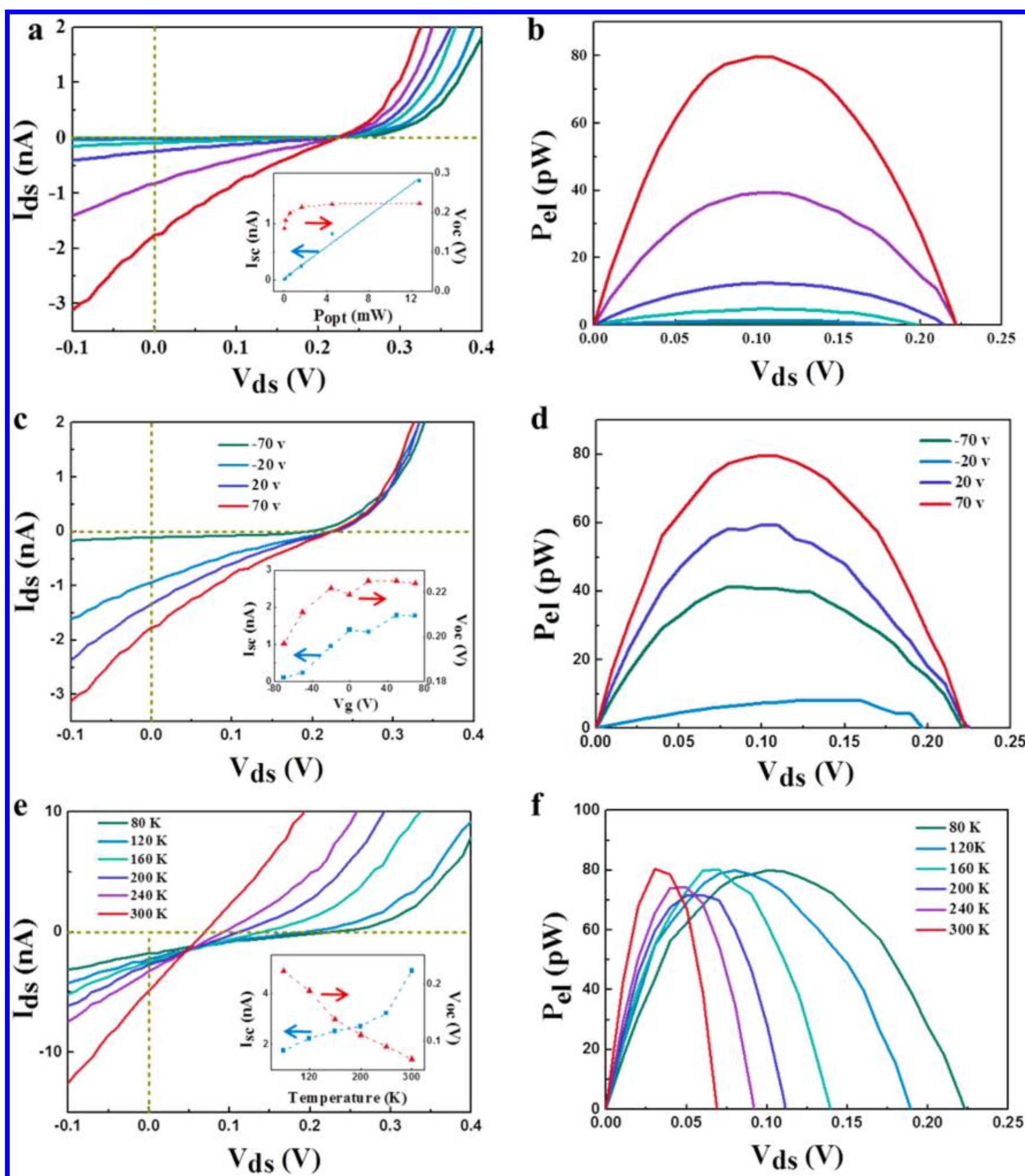

Figure 4. (a) Current−voltage characteristics under illumination with light powers of 0.04, 0.148, 0.563, 1.638, 4.54, and 12.77 mW (from green to red), respectively. V_{ds} and I_{ds} = 0 are marked as dashed yellow lines. The inset shows the short-circuit currents (I_{sc}, blue symbols) and open-circuit voltages (V_{oc}, red symbols) as a function of light power density. The blue line is the linear fit of I_{sc}−P_{opt}. (b) The electrical powers (extracted from a, defined as $P_{el} = I_{ds}V_{ds}$)−voltage curves under various illumination power densities. The measurement was taken at 80 K using a 473 nm laser as the light source. (c) Current−voltage characteristics at various gate voltages, while temperature was 80 K. Inset: Short-circuit currents (blue symbols) and open-circuit voltages (red symbols) as a function of gate voltage. The corresponding electrical power-voltage curves are shown in (d). (e) Current−voltage characteristics at different temperatures with constant gate voltage V_g = 70 V. Inset: Short-circuit currents (blue symbols) and open-circuit voltages (red symbols) as a function of temperature. The corresponding electrical power−voltage curves are shown in (f). A 473 nm laser with a power of 12.77 mW was used as the light source for (c−f).

composed of MoS_2 and GaTe with few-layer thickness, which perhaps induces a different mechanism behind the electronic behavior. Further studies on vdW heterostructures with different 2D semiconductors as well as different thicknesses are needed. Note that the IF values of higher than 2 may arise from the defects, including both fixed charge impurities on SiO_2 substrates as well as polymer and water residues at GaTe/MoS_2 interfaces.[46−48]

Based on the rectification characteristics shown above, we next studied the light power-, V_g-, and T-tunable PV effect of the vdW p−n junction. A 473 nm laser with spot diameter of 5 mm was used as the light source. In Figure 4a, we present the I_{ds}−V_{ds} curves (measured at V_g = 70 V and T = 80 K) with the incident light power (P_{opt}) varied from 0.04 to 12.77 mW (0.2 to 65.1 mW/cm^2), from which we can see an obvious PV effect for all of the P_{opt} values. The extracted short-circuit current (I_{sc}), open-circuit voltage (V_{oc}), and electrical powers[34] (P_{el},

DOI: 10.1021/acs.nanolett.5b03291
Nano Lett. XXXX, XXX, XXX−XXX

defined as $P_{el} = I_{ds}V_{ds}$) are given in the insets of Figure 4a,b, respectively. As we can see, as P_{opt} increases V_{oc} increases initially and reaches saturation almost immediately. However, I_{sc} increases linearly and no saturation is found over the test range. By fitting I_{sc} and P_{opt} data with a double-logarithmic scale (Figure S5a, Supporting Information), the I_{sc} follows the power-law dependence of $I_{sc} = P_{opt}^{\alpha}$ with scaling exponent $\alpha \approx 0.93$. In addition, by fitting V_{oc} and P_{opt} in a single-logarithmic scale (Figure S5b, Supporting Information), the I_{sc} follows the power-law dependence of $(dV_{oc}/d\ln(P_{opt})) = n_{voc}2.3(k_BT/q)$ with $n_{voc} \approx 1.9$ (where k_B is Boltzman's constant, T is the temperature, and q is the elementary charge). Both the nearly linear dependence of I_{sc} and the n_{voc} value of approximately 2 indicate that the first order recombination (e.g., Shockley Read Hall; SRH recombination) dominated the carrier loss during transport.[36,37] In other words, there was a large density of defects/trap states in our junction, which probably came from the MoS_2/GaTe interface (such as polymer and water residues) and/or surfaces of these two materials (such as the interfaces between the materials and the SiO_2 substrates). This conforms to the finding that 2D materials, like MoS_2, are governed by VRH transport mechanism, which is usually used in strongly disordered systems.[33] To improve the PV effect of 2D vdWHs, a process for a clean interface and weak interface scattering is needed.

Then, V_g-dependent PV effect was studied with P_{opt} and T set to 12.77 mW and 80 K. Figure 4c shows the I_{ds}−V_{ds} characteristics, and the V_g-dependent I_{sc}, V_{oc}, and P_{el} are extracted and given in the insets of Figure 4c,d, respectively. It is apparent that all of them increase monotonically with increasing V_g and maximums of ~1.8 nA, ~ 224 mV, and ~80 pW achieved at V_g = 70 V. This observation reflects the electronic behavior shown above, which can also be understood by considering the band diagrams under a forward bias shown in Figure 3 and before contact in Figure S8 (Supporting Information). For ideal solar cells, $V_{oc} = ((|E_{F_p} - E_{F_n}|)/q)$, where E_{Fn} and E_{Fp} are the quasi-Fermi levels of n- and p-type semiconductors under steady-state illumination, respectively.[49] Hence, the V_{oc} can be controlled by the ΔE_F. In our device, due to the specific band positions, a negative/positive V_g gave rise to smaller/higher ΔE_F between GaTe and MoS_2, i.e., a smaller/higher V_{oc}. Although the value of loading resistance might reach a valley at V_g = −20 V (because of the peak of carrier densities shown above), the trend of V_{oc} dominated over the other factors. As a result, all of these characteristic values (V_{oc}, I_{sc}, and P_{el}) exhibited their maximized values at V_g = 70 V.

In addition, T-dependent I_{ds}−V_{ds} curves measured at V_g = 70 V are presented in Figure 4e. The corresponding I_{sc}, V_{oc}, and P_{el} are extracted and shown in the insets of Figure 4e,f. Unlike the relationships with V_g, the I_{sc} and V_{oc} vary in opposite directions as T increases from 80 to 300 K, and a roughly constant P_{el} results. Qualitatively, as T increases, the charge densities increased accompany and the E_Fs approached their respective intrinsic Fermi levels (E_i) (as shown in Figure 3c), giving a lower V_{oc}. Quantitatively, in a nondegenerate semiconductor (which is appropriate for our p−n junction due to the low carrier densities), $V_{oc} = ((E_{gef} - k_BT\ln(N_cN_v/np))/q)$, where E_{gef} is the effective band gap (here $E_{gef} = E_{cMoS2} - E_{vGaTe}$), and N_c, n and N_v, p are the effective densities of states and carrier densities for MoS_2 and GaTe, respectively.[49] From this equation, we can see that as T increase and V_{oc} decreases. By fitting the V_{oc}−T line shown in the inset of Figure 4e, an open circuit voltage temperature coefficient $(dV_{oc}/dT) \approx -0.7$ mV/K is extracted. In addition, from the measured V_{oc} (0.063 V) at 300 K and V_g = 0 V (Figure S7, Supporting Information), we can estimate the ΔE_F to be approximately 0.1 eV, which agrees highly with Figure 1b. However, the loading resistance decreased more significantly due to the increasing mobility and/or charge carrier densities, which resulted in the opposite trend for I_{sc} and a roughly constant P_{el}. Interestingly, the fill factor (FF), defined as $FF = P_{el,\,max}/I_{sc}V_{oc}$,[34] where $P_{el,\,max}$ is the maximum of P_{el}, can also be tuned by P_{opt}, V_g and T, as shown in Figure S9 (Supporting Information). A highest FF of 0.42 is obtained at V_g = −50 V and T = 80 K.

The photoresponse properties of our p−n junction as a photodetector were also studied. Figure 5a displays the relationships between I_{ph} and incident light power under various V_g (V_{ds} = 1 V, T = 80 K). The I_{ph} exhibits a strong dependence on V_g, and the maximum I_{ph} appears at V_g = −70 V. This is probably due to the minimum potential barrier (resulting from the minimum ΔE_F) for photostimulated charge carriers going through the p−n junction region at this V_g. In addition, the I_{ph} increases monotonically with increasing P_{opt}, giving rise to dependences of $I_{ph} \approx P_{opt}^{\alpha}$, with α = 0.24, 0.19, 0.36, 0.16, and 0.09 for V_g = 70, 20, 0, −20, and −70 V, respectively. The linear relationships demonstrate that the density of photogenerated carriers is proportional to the

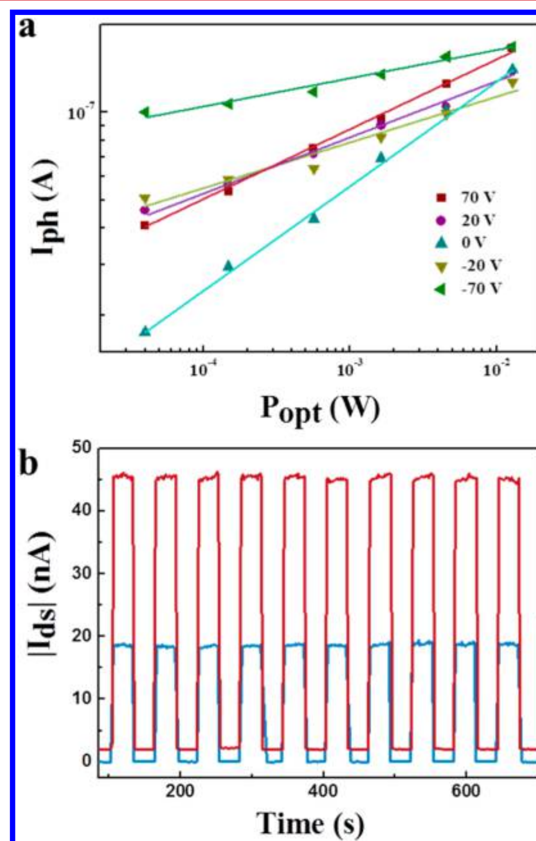

Figure 5. (a) Photocurrents under various light intensities with different gate voltages. The fitting lines give the relationships of $I_{ph} \approx P_{opt}^{\alpha}$, with α = 0.24, 0.19, 0.36, 0.16, and 0.09 for V_g = 70, 20, 0, −20, and −70 V, respectively. V_{ds} = 1 V and T = 80 K. (b) The time-dependent photoresponse characteristics at 300 K (red line) and 80 K (blue line), respectively. V_{ds} = −1 V and V_g = 0 V. A 473 nm laser with P_{opt} = 12.77 mW used as the light source.

DOI: 10.1021/acs.nanolett.5b03291
Nano Lett. XXXX, XXX, XXX−XXX

Table 1. Calculated Photovoltaic and Photoresponse Performance Metrics, Including Fill Factor (FF), External Quantum Efficiency (EQE), Energy Conversion Efficiency (η), Photoresponsivity (R_{ph}), and Optical Gain (G) at V_g = 70/−70 V and T = 80/300 K; a 473 nm Laser with P_{opt} = 12.77 mW Was Used as the Light Source

	figure of merits (at V_g = 70/−70 V)				
T (K)	FF	EQE (%)	η (%)	R_{ph} (A/W)	G (%)
80	0.21/0.39	26.21/1.60	0.45/0.05	9.41/9.53	2473/2505
300	0.25/0.28	61.68/1.34	0.42/0.003	21.83/11.20	5737/2944

Table 2. Comparison of the Photovoltaic and Photoresponse Performance Metrics of Our GaTe/MoS_2 van der Waals p−n Junction with Other 2D Heterostructures; the Highest Values Are Extracted and Used Here

devices	thickness	FF	EQE (%)	η (%)	R_{ph} ($A W^{-1}$)	detectivity (Jones)	ref
MoS_2/WSe_2	multilayer/multilayer		∼40		∼0.125		6
MoS_2/WSe_2	monolayer/monolayer	∼0.5	1.5	0.2	0.011		21
BP/MoS_2	11 nm/monolayer	0.5	0.3		3.54		22
MoS_2/WS_2	multilayer/multilayer				1.42		23
MoS_2/MoS_2	2−60 nm				5.07	3×10^{10}	24
MoS_2/MoS_2	11 nm	0.22			0.03		58
GaTe/MoS_2	14.1/5.5 nm	0.42	61.68	0.45	21.83	8.4×10^{13}	present work

absorbed light. However, the deviation of α from 1 indicates the loss of photostimulated carriers, again demonstrating that there are a large amount of trap states (defects) in 2DLMs and vdWHs.[27] We also evaluated the photoresponse performance by calculating photoresponsivity (R_{ph}) and photogain (G) through the following equations:[50]

$$R_{ph} = I_{ph}/PA$$

$$G = R_{ph}\frac{hc}{q\lambda}$$

where $I_{ph} = I_{photo} - I_{dark}$, I_{photo} and I_{dark} are the drain currents with and without incident light, respectively, A is the effective area, and P is the light density (assume that the incident light was all absorbed). Table 1 gives the calculated values using a constant incident laser power of 12.77 mW. Note that the sublinearity between I_{ph} and P_{opt} shown in Figure 5a and high gains (more than 1) have also been found in other materials, such as ZnO nanowires,[51] GaN homojunction,[52] few-layer GaTe,[34] monolayer MoS_2,[28] etc. The high gain of our van der Waals p−n junction is probably due to the increased lifetime of photogenerated carriers that are separated by the built-in potential,[51−53] and the inconsistency between the high gain and the sublinearity of I_{ph}−P_{opt} is probably attributed to the persistent photocurrent.[52,54] Another important parameter to quantify the photoresponse property is the specific detectivity (D^*), $D^* = (A\Delta f)^{1/2}/NEP$, where A is the effective area of the detector in cm^2, Δf is the electrical bandwidth in Hz, and NEP is the noise equivalent power. By assuming that the dark current is the major contributor to shot noise, D^* can be expressed as $D^* = I_{ph}A^{1/2}/PA(2qI_{dark})^{1/2}$.[38,55] Based on the measured parameters, D^* values of approximately 8.4×10^{13} and 5.7×10^{13} Jones are achieved at V_g = 70 V and −70 V (T = 80 K, see Supporting Information for details). Figure 5b shows the time dependence of I_{ds} while V_{ds} = −1 V measured at both 80 K (red line) and 300 K (blue line). Due to the ultralow dark current under the reverse bias condition, good photoresponse performance was achieved for both temperatures. Furthermore, the photoswitching on/off ratio (define as I_{photo}/I_{dark}) reached as high as 10^3 at 80 K. The time-resolved photoresponse performance was also studied, and a response time of less than 7 ms was detected (see Supporting Information for details).

On the basis of the previously discussed optoelectronic properties of the GaTe/MoS_2 van der Waals p−n junction, we evaluated the photovoltaic performance by calculating the external quantum efficiency (EQE) and photon to current conversion efficiency (η) by the following equations:[34]

$$EQE(\%) = \frac{I_{SC}}{PA_q}\frac{hc}{\lambda} \times 100$$

and

$$\eta = P_{el,max}/PA$$

where h, c, and λ are Planck's constant, the speed of light, and the wavelength of light, respectively. Table 1 gives the calculated values at V_g = 70/−70 V, respectively (see Supporting Information for details). It is noteworthy that an EQE as high as 61.68% was achieved (V_g = 70 V at 300 K), which is the highest value reported for van der Waals heterostructures. Table 2 summarizes and compares the selected figures of merit between the GaTe/MoS_2 p−n junction and several other reported two-dimensional layered heterostructures. The high optoelectronic performance of GaTe/MoS_2 van der Waals heterostructure is clear from this summary of results. The high optoelectronic performance is probably due to (a) the novel optoelectronic properties of both MoS_2[56] and, more importantly, GaTe (as high as 10^4 A/W);[28] (b) intrinsic p-type GaTe and n-type MoS_2, which do not suffer from scattering of exotic dopants; (c) a type II band gap alignment, which promotes the separation of photostimulated charge carriers; and (d) the few-layer thickness, which provides better screening against the Coulomb scattering.[57]

In summary, tunable electronic and optoelectronic properties based on GaTe/MoS_2 van der Waals p−n junction were demonstrated. The rectification effects, photovoltaic ability, and photodetection properties were carefully investigated at various temperatures, electrical gate biases, and light intensities. The p−n junctions showed strong gate- and temperature-tunable rectification characteristics and photovoltaic effects. For the photovoltaic effect, an SRH mechanism dominated the interlayer recombination, and an open circuit voltage temperature coefficient of (dV_{oc}/dT) ≈ −0.7 mV/K was demonstrated. Furthermore, an external quantum efficiency as high as 61.68% was achieved. In addition, the GaTe/MoS_2 p−n

DOI: 10.1021/acs.nanolett.5b03291
Nano Lett. XXXX, XXX, XXX−XXX

junction exhibited good photodetection performance with room-temperature responsivity and a photogain of 21.83 A W^{-1} and 5737%, respectively. Remarkably, a selective detectivity of 8.4×10^{13} Jones was achieved, which is even higher than commercial Si/InGaAs photodetectors. All these notable performance metrics demonstrate the potential applications of GaTe/MoS_2 van der Waals p−n junction in both electronic and optoelectronic devices.

Methods. *Device Fabrication.* The devices were fabricated by mechanical exfoliation and a targeted transfer method. Few-layer MoS_2 was exfoliated from the bulk crystal (purchased form SPI) onto Si wafers with 300 nm SiO_2, which had been cleaned with a piranha solution for 2 h. Then, the wafer was annealed under vacuum (10^{-1} Torr) at 300 °C for 3 h to remove any residue tapes. The thickness of the MoS_2 was verified by OM and AFM. After that, PVA and PMMA were sequentially spin-coated on the top of another SiO_2/Si substrate. GaTe (99.99%, Alfa Aesar) was then exfoliated onto the SiO_2/PVA/PMMA substrate. After dissolving the PVA in DI-water, the PMMA film carrying exfoliated GaTe was floated and then mounted on the arm of a micromanipulator. With the help of OM, GaTe was transferred directionally to the target MoS_2 flake. During the transfer, the target wafer was heated to 180 °C to ensure a good adhesion between the PMMA and the bottom wafer. The PMMA was then dissolved by soaking the wafer in acetone. Finally, the heterostructure was again annealed under vacuum at 160 °C for 6 h again to eliminate any possible contamination from the MoS_2/GaTe interface. Electrode patterns were defined by standard EBL, and 8/60 nm Cr/Au electrodes were deposited by thermal evaporation.

Device Characterization. The morphology, material quality, and thickness characterizations were performed by OM (Olympus BX51 M), Raman spectroscopy (Renishaw InVia, 532 nm excitation laser), and AFM (Veeco Multimode), respectively. The electrical transport measurements were carried out on a probe station (Lakeshore, TTP4) equipped with a vacuum pump, a flow cryostat, and a semiconductor characterization system (Keithley 4200). The optoelectronic properties were measured using a 473 nm laser with a diameter of 5 mm and maximum light intensity of 12.77 mW (RGBLase). The light intensity was varied using a continuous attenuator.

■ ASSOCIATED CONTENT

Ⓢ Supporting Information

The Supporting Information is available free of charge on the ACS Publications website at DOI: 10.1021/acs.nanolett.5b03291.

Detailed schematic crystal structures of MoS_2 and GaTe, the Raman spectra, a calculation of the band positions, additional electronic and optoelectronic characterization of the GaTe/MoS_2 van der Waals p−n junction, and further calculation details (PDF)

■ AUTHOR INFORMATION

Corresponding Author

*E-mail: hej@nanoctr.cn.

Notes

The authors declare no competing financial interest.

■ ACKNOWLEDGMENTS

This work was conducted at the National Center for Nanoscience and Technology and supported by the 973 Program of the Ministry of Science and Technology of China (No. 2012CB934103), the 100-Talents Program of the Chinese Academy of Sciences (No. Y1172911ZX), the National Natural Science Foundation of China (Nos. 21373065 and 61474033), and the Beijing Natural Science Foundation (No. 2144059).

■ REFERENCES

(1) Geim, A. K.; Grigorieva, I. V. *Nature* **2013**, *499* (7459), 419−425.
(2) Wang, H.; Liu, F. C.; Fu, W.; Fang, Z. Y.; Zhou, W.; Liu, Z. *Nanoscale* **2014**, *6* (21), 12250−12272.
(3) Roy, T.; Tosun, M.; Kang, J. S.; Sachid, A. B.; Desai, S. B.; Hettick, M.; Hu, C. M. C.; Javey, A. *ACS Nano* **2014**, *8* (6), 6259−6264.
(4) Yu, W. J.; Liu, Y.; Zhou, H. L.; Yin, A. X.; Li, Z.; Huang, Y.; Duan, X. F. *Nat. Nanotechnol.* **2013**, *8* (12), 952−958.
(5) Britnell, L.; Gorbachev, R. V.; Jalil, R.; Belle, B. D.; Schedin, F.; Mishchenko, A.; Georgiou, T.; Katsnelson, M. I.; Eaves, L.; Morozov, S. V.; Peres, N. M. R.; Leist, J.; Geim, A. K.; Novoselov, K. S.; Ponomarenko, L. A. *Science* **2012**, *335* (6071), 947−950.
(6) Lee, C. H.; Lee, G. H.; van der Zande, A. M.; Chen, W. C.; Li, Y. L.; Han, M. Y.; Cui, X.; Arefe, G.; Nuckolls, C.; Heinz, T. F.; Guo, J.; Hone, J.; Kim, P. *Nat. Nanotechnol.* **2014**, *9* (9), 676−681.
(7) Georgiou, T.; Jalil, R.; Belle, B. D.; Britnell, L.; Gorbachev, R. V.; Morozov, S. V.; Kim, Y. J.; Gholinia, A.; Haigh, S. J.; Makarovsky, O.; Eaves, L.; Ponomarenko, L. A.; Geim, A. K.; Novoselov, K. S.; Mishchenko, A. *Nat. Nanotechnol.* **2012**, *8* (2), 100−103.
(8) Sup Choi, M.; Lee, G. H.; Yu, Y. J.; Lee, D. Y.; Lee, S. H.; Kim, P.; Hone, J.; Yoo, W. J. *Nat. Commun.* **2013**, *4*, 1624.
(9) Fang, H.; Battaglia, C.; Carraro, C.; Nemsak, S.; Ozdol, B.; Kang, J. S.; Bechtel, H. A.; Desai, S. B.; Kronast, F.; Unal, A. A.; Conti, G.; Conlon, C.; Palsson, G. K.; Martin, M. C.; Minor, A. M.; Fadley, C. S.; Yablonovitch, E.; Maboudian, R.; Javey, A. *Proc. Natl. Acad. Sci. U. S. A.* **2014**, *111* (17), 6198−6202.
(10) Cheng, R.; Li, D. H.; Zhou, H. L.; Wang, C.; Yin, A. X.; Jiang, S.; Liu, Y.; Chen, Y.; Huang, Y.; Duan, X. F. *Nano Lett.* **2014**, *14* (10), 5590−5597.
(11) Mak, K. F.; Lee, C.; Hone, J.; Shan, J.; Heinz, T. F. *Phys. Rev. Lett.* **2010**, *105*, 136805.
(12) Xu, M. S.; Liang, T.; Shi, M. M.; Chen, H. Z. *Chem. Rev.* **2013**, *113* (5), 3766−3798.
(13) Tongay, S.; Sahin, H.; Ko, C.; Luce, A.; Fan, W.; Liu, K.; Zhou, J.; Huang, Y. S.; Ho, C. H.; Yan, J. Y.; Ogletree, D. F.; Aloni, S.; Ji, J.; Li, S. S.; Li, J. B.; Peeters, F. M.; Wu, J. Q. *Nat. Commun.* **2014**, *5*, 3252.
(14) Kang, J.; Tongay, S.; Zhou, J.; Li, J. B.; Wu, J. Q. *Appl. Phys. Lett.* **2013**, *102* (1), 012111.
(15) Jiang, H. *J. Phys. Chem. C* **2012**, *116* (14), 7664−7671.
(16) Hong, X. P.; Kim, J.; Shi, S. F.; Zhang, Y.; Jin, C. H.; Sun, Y. H.; Tongay, S.; Wu, J. Q.; Zhang, Y. F.; Wang, F. *Nat. Nanotechnol.* **2014**, *9* (9), 682−686.
(17) Huang, C. M.; Wu, S. F.; Sanchez, A. M.; Peters, J. J. P.; Beanland, R.; Ross, J. S.; Rivera, P.; Yao, W.; Cobden, D. H.; Xu, X. D. *Nat. Mater.* **2014**, *13* (12), 1096−1101.
(18) Duan, X. D.; Wang, C.; Shaw, J. C.; Cheng, R.; Chen, Y.; Li, H. L.; Wu, X. P.; Tang, Y.; Zhang, Q. L.; Pan, A. L.; Jiang, J. H.; Yu, R. Q.; Huang, Y.; Duan, X. F. *Nat. Nanotechnol.* **2014**, *9* (12), 1024−1030.
(19) Tongay, S.; Fan, W.; Kang, J.; Park, J.; Koldemir, U.; Suh, J.; Narang, D. S.; Liu, K.; Ji, J.; Li, J. B.; Sinclair, R.; Wu, J. Q. *Nano Lett.* **2014**, *14* (6), 3185−3190.
(20) Zhang, X. Q.; Lin, C. H.; Tseng, Y. W.; Huang, K. H.; Lee, Y. H. *Nano Lett.* **2015**, *15* (1), 410−415.
(21) Furchi, M. M.; Pospischil, A.; Libisch, F.; Burgdorfer, J.; Mueller, T. *Nano Lett.* **2014**, *14* (8), 4785−4791.

(22) Deng, Y. X.; Luo, Z.; Conrad, N. J.; Liu, H.; Gong, Y. J.; Najmaei, S.; Ajayan, P. M.; Lou, J.; Xu, X. F.; Ye, P. D. *ACS Nano* **2014**, *8* (8), 8292−8299.
(23) Huo, N. J.; Kang, J.; Wei, Z. M.; Li, S. S.; Li, J. B.; Wei, S. H. *Adv. Funct. Mater.* **2014**, *24* (44), 7025−7031.
(24) Choi, M. S.; Qu, D.; Lee, D.; Liu, X.; Watanabe, K.; Taniguchi, T.; Yoo, W. J. *ACS Nano* **2014**, *8* (9), 9332−9340.
(25) Radisavljevic, B.; Radenovic, A.; Brivio, J.; Giacometti, V.; Kis, A. *Nat. Nanotechnol.* **2011**, *6* (3), 147−150.
(26) Radisavljevic, B.; Kis, A. *Nat. Mater.* **2013**, *12* (9), 815−820.
(27) Yin, Z. Y.; Li, H.; Li, H.; Jiang, L.; Shi, Y. M.; Sun, Y. H.; Lu, G.; Zhang, Q.; Chen, X. D.; Zhang, H. *ACS Nano* **2012**, *6* (1), 74−80.
(28) Zhang, W. J.; Huang, J. K.; Chen, C. H.; Chang, Y. H.; Cheng, Y. J.; Li, L. J. *Adv. Mater.* **2013**, *25* (25), 3456−3461.
(29) Li, H.; Wu, J. M. T.; Yin, Z. Y.; Zhang, H. *Acc. Chem. Res.* **2014**, *47* (4), 1067−1075.
(30) Huang, X.; Zeng, Z. Y.; Zhang, H. *Chem. Soc. Rev.* **2013**, *42* (5), 1934−1946.
(31) Baugher, B. W. H.; Churchill, H. O. H.; Yang, Y. F.; Jarillo-Herrero, P. *Nat. Nanotechnol.* **2014**, *9* (4), 262−267.
(32) Pospischil, A.; Furchi, M. M.; Mueller, T. *Nat. Nanotechnol.* **2014**, *9* (4), 257−261.
(33) Lin, Y. F.; Xu, Y.; Wang, S. T.; Li, S. L.; Yamamoto, M.; Aparecido-Ferreira, A.; Li, W. W.; Sun, H. B.; Nakaharai, S.; Jian, W. B.; Ueno, K.; Tsukagoshi, K. *Adv. Mater.* **2014**, *26* (20), 3263.
(34) Wang, Z. X.; Xu, K.; Li, Y. C.; Zhan, X. Y.; Safdar, M.; Wang, Q. S.; Wang, F. M.; He, J. *ACS Nano* **2014**, *8* (5), 4859−4865.
(35) Liu, F. C.; Shimotani, H.; Shang, H.; Kanagasekaran, T.; Zolyomi, V.; Drummond, N.; Fal'ko, V. I.; Tanigaki, K. *ACS Nano* **2014**, *8* (1), 752−760.
(36) Cheyns, D.; Poortmans, J.; Heremans, P.; Deibel, C.; Verlaak, S.; Rand, B. P.; Genoe, J. *Phys. Rev. B: Condens. Matter Mater. Phys.* **2008**, *77* (16), 165332.
(37) Riedel, I.; Parisi, J.; Dyakonov, V.; Lutsen, L.; Vanderzande, D.; Hummelen, J. C. *Adv. Funct. Mater.* **2004**, *14* (1), 38−44.
(38) Zhang, W.; Chiu, M. H.; Chen, C. H.; Chen, W.; Li, L. J.; Wee, A. T. S. *ACS Nano* **2014**, *8* (8), 8653−8661.
(39) Gong, X.; Tong, M. H.; Xia, Y. J.; Cai, W. Z.; Moon, J. S.; Cao, Y.; Yu, G.; Shieh, C. L.; Nilsson, B.; Heeger, A. J. *Science* **2009**, *325* (5948), 1665−1667.
(40) Dean, C. R.; Young, A. F.; Meric, I.; Lee, C.; Wang, L.; Sorgenfrei, S.; Watanabe, K.; Taniguchi, T.; Kim, P.; Shepard, K. L.; Hone, J. *Nat. Nanotechnol.* **2010**, *5* (10), 722−726.
(41) Zhou, W. C.; Zhou, Y.; Peng, Y. H.; Zhang, Y.; Yin, Y. L.; Tang, D. S. *Nanotechnology* **2014**, *25* (44), 445202.
(42) Gong, C.; Colombo, L.; Wallace, R. M.; Cho, K. *Nano Lett.* **2014**, *14* (4), 1714−1720.
(43) Li, H.; Zhang, Q.; Yap, C. C. R.; Tay, B. K.; Edwin, T. H. T.; Olivier, A.; Baillargeat, D. *Adv. Funct. Mater.* **2012**, *22* (7), 1385−1390.
(44) Ghatak, S.; Pal, A. N.; Ghosh, A. *ACS Nano* **2011**, *5* (10), 7707−7712.
(45) Neamen, D. A.; Pevzner, B. *Semiconductor Physics and Devices: Basic Principles*; McGraw-Hill: New York, 2003; Vol. 3.
(46) Shah, J. M.; Li, Y. L.; Gessmann, T.; Schubert, E. F. *J. Appl. Phys.* **2003**, *94* (4), 2627−2630.
(47) Wang, C. X.; Yang, G. W.; Liu, H. W.; Han, Y. H.; Luo, J. F.; Gao, C. X.; Zou, G. T. *Appl. Phys. Lett.* **2004**, *84* (13), 2427−2429.
(48) Breitenstein, O.; Altermatt, P.; Ramspeck, K.; Schenk, A. The origin of ideality factors n > 2 of shunts and surfaces in the dark IV curves of Si solar cells. In *Proceedings of the 21st European Photovoltaic Solar Energy Conference*, 2006; pp 625−628.
(49) Garcia-Belmonte, G. *Sol. Energy Mater. Sol. Cells* **2010**, *94* (12), 2166−2169.
(50) Koppens, F. H. L.; Mueller, T.; Avouris, P.; Ferrari, A. C.; Vitiello, M. S.; Polini, M. *Nat. Nanotechnol.* **2014**, *9* (10), 780−793.
(51) Soci, C.; Zhang, A.; Xiang, B.; Dayeh, S. A.; Aplin, D. P. R.; Park, J.; Bao, X. Y.; Lo, Y. H.; Wang, D. *Nano Lett.* **2007**, *7* (4), 1003−1009.
(52) Gonzalez-Posada, F.; Songmuang, R.; Den Hertog, M.; Monroy, E. *Nano Lett.* **2012**, *12* (1), 172−176.
(53) Konstantatos, G.; Badioli, M.; Gaudreau, L.; Osmond, J.; Bernechea, M.; de Arquer, F. P. G.; Gatti, F.; Koppens, F. H. L. *Nat. Nanotechnol.* **2012**, *7* (6), 363−368.
(54) Monroy, E.; Omnes, F.; Calle, F. *Semicond. Sci. Technol.* **2003**, *18* (4), R33−R51.
(55) Manga, K. K.; Wang, S.; Jaiswal, M.; Bao, Q. L.; Loh, K. P. *Adv. Mater.* **2010**, *22* (46), 5265−5270.
(56) Lopez-Sanchez, O.; Lembke, D.; Kayci, M.; Radenovic, A.; Kis, A. *Nat. Nanotechnol.* **2013**, *8* (7), 497−501.
(57) Kim, S.; Konar, A.; Hwang, W. S.; Lee, J. H.; Lee, J.; Yang, J.; Jung, C.; Kim, H.; Yoo, J. B.; Choi, J. Y.; Jin, Y. W.; Lee, S. Y.; Jena, D.; Choi, W.; Kim, K. *Nat. Commun.* **2012**, *3*, 1011.
(58) Li, H.-M.; Lee, D.; Qu, D.; Liu, X.; Ryu, J.; Seabaugh, A.; Yoo, W. J. *Nat. Commun.* **2015**, *6*, 6564.

DOI: 10.1021/acs.nanolett.5b03291
Nano Lett. XXXX, XXX, XXX−XXX